

Article

Structural, Hirshfeld Surface Analysis, Morphological Approach, and Spectroscopic Study of New Hybrid Iodobismuthate Containing Tetranuclear 0D Cluster $\text{Bi}_4\text{I}_{16}\cdot 4(\text{C}_6\text{H}_9\text{N}_2) 2(\text{H}_2\text{O})$

Hela Ferjani

Chemistry Department, College of Science, IMSIU (Imam Mohammad Ibn Saud Islamic University), Riyadh 11623, Saudi Arabia; hhferjani@imamu.edu.sa

Received: 20 April 2020; Accepted: 13 May 2020; Published: 15 May 2020



Abstract: The $\text{Bi}_4\text{I}_{16}\cdot 4(\text{C}_6\text{H}_9\text{N}_2) 2(\text{H}_2\text{O})$ compound was synthesized by slow evaporation at room temperature. It exhibits a zero-dimensional (0D) tetrameric structure, comprising $[\text{Bi}_4\text{I}_{16}]^{4-}$ distorted octahedra, with strong $\text{I}\cdots\text{I}$ interactions among adjacent anionic clusters. We used Hirshfeld surface analysis to discuss the strength of hydrogen bonds and to quantify the inter-contacts (two-dimensional (2D) fingerprint plots). It revealed that the hydrogen bonding interactions $\text{H}\cdots\text{I}$ (56.3%), π - π stacking (11.7%), and $\text{I}\cdots\text{I}$ interactions (5.9%) play the major role in the stability of the crystal structure. The crystal morphology was simulated using Bravais–Friedel, Donnay–Harker (BFDH) and growth morphology (GM) methods. The experimental habit of the title compound was adequately reproduced by the two models. The calculated results show that the crystal morphology of the title compound in a vacuum is dominated by five facets: (020), (011), (110), (10–1), and (11–1). The (020) facet is the largest among all the facets calculated. Projection of the facet showed that there are a few polar groups on the (020) facet. In the 50–400 and 400–4000 cm^{-1} frequency regions, we measured the Raman and infrared spectra, respectively, of the title compound, and we assigned the observed vibration modes.

Keywords: iodobismuthate; tetranuclear cluster; 1-allylimidazole; crystal morphology; Hirshfeld surface analysis; infrared and Raman spectroscopy

1. Introduction

As a significant type of hybrid material, organic–inorganic hybrid materials (OIHM) based on halogenometallates attracted remarkable attention in recent years, due to their structural diversity and several physical properties arising from the mixture between organic and inorganic parts. Many studies concentrated on the synthesis and characterization of such materials [1–6]. However, hybrid materials based on bismuth were paid special attention owing to their diverse structures, developing a variety of ferroelectric and Ferro-elastic devices [7–11], with novel thermochromic, optical, and electrical properties [12–15]. Halogenobismuthate (III)-based materials occupy an exceptional place for the replacement of lead-based compounds in photovoltaic cells [16–19]. These compounds are unaffected by humidity like lead compounds. According to the literature, these materials can exhibit a great diversity of anionic sublattices built from different linkages of BiX_6 ($X = \text{Cl}, \text{Br}, \text{and I}$) octahedra including corner-, edge-, or face-sharing modes [20–26]. Furthermore, the supramolecular assemblies of halogenobismuthate compounds depend on some parameters, such as bonds, coordination geometries around the metal center, the nature of the ligands, the metal–ligand stoichiometry, and the different experimental conditions such as solvents, temperature, the concentration of hydro-halogenic acid, and crystallization methods. For instance, this complex presents the new salt isolated by 1-allylimidazole in the crystalline state from diluted HI. From the Cambridge Crystallographic Database, 1-allylimidazole

is a good template that is rarely studied, presenting both rigidity and flexibility. In recent times, flexible and rigid organic templates were often used to build interesting structures due to their influence on the arrangement of the inorganic networks. It is worth mentioning that the supramolecular arrangement is controlled by different kinds of electrostatic interactions such as hydrogen bonds, π - π interactions, and halogen...halogen contacts. Thus, to examine these interactions inside the supramolecular arrangement, it is important to study their quantitative measurements.

Here, we report the synthesis of new perovskite-like hybrid iodobismuthate $\text{Bi}_4\text{I}_{16}\cdot 4(\text{C}_6\text{H}_9\text{N}_2) 2(\text{H}_2\text{O})$. We discuss the crystal structure and the spectroscopic behavior. The intermolecular interactions were described by Hirshfeld surface analysis. The theoretical crystal morphology was calculated showing a big similarity with the experimental one.

2. Materials and Methods

2.1. Synthesis

Crystals of $\text{Bi}_4\text{I}_{16}\cdot 4(\text{C}_6\text{H}_9\text{N}_2) 2(\text{H}_2\text{O})$ were synthesized by slow evaporation at room temperature. Firstly, we dissolved, in an aqueous solution, 1-allylimidazole (0.3 g, 2 mmol) and HI (3 mL of H_2O and 2 mL of HI, 57%). Then, Bi_2O_3 (0.65 g, 1 mmol) was dissolved in 10 mL of H_2O and 5 mL of HI and stirred for 30 min. The two solutions were mixed together and stirred for four hours with heating (50 °C). The saturated orange solution was put in the dark for evaporation at room temperature. After three days, block orange crystals were formed.

2.2. Crystal Data and Structure Determination

A Bruker D8 Quest (Madison, WI, USA) diffractometer (MoK_α radiation $\lambda = 0.71073 \text{ \AA}$) was used to collect the single-crystal X-ray data at 298 K, via the Bruker APEX3 software package [27]. SAINT [28] was executed for data reduction. Multi-scan absorption correction was accomplished using SADABS [29]. The SHELXS (Madison, WI, USA) and SHELXTL (Madison, WI, USA) packages were used to solve the structure via direct methods, and the program SHELXL-2014 was performed to refine the structure using full-matrix least squares procedures on F^2 [30]. All non-hydrogen atoms were refined with anisotropic displacement parameters. Hydrogen atoms were located at calculated positions using a riding model. We could not locate the hydrogen atoms of water molecules but we included them in the formula. Diamond 3 was used to prepare the molecular graphics [31]. Table 1 shows details of the data collection and crystallographic parameters. Table S1 (Supplementary Materials) provides the atomic coordinates and equivalent isotropic displacement parameters. Some interatomic distances and bond angles are given in Table 2.

2.3. Physicochemical Characterization

A Nicolet NXR Fourier-transform infrared (FT-IR) spectrometer (Dhahran, Saudi Arabia) was used to record the FT-IR spectrum in the 400–4000 cm^{-1} region at room temperature on a KBr disc. The Raman spectrum was recorded using a HORIBA Lab RAM HR Evolution Surface-Enhanced Raman Scattering Microscope (Dhahran, Saudi Arabia) in the 400–50 cm^{-1} region. The morphology of the sample was observed using a JEOL, JSM-6380-LA electron microscope (Riyadh, Saudi Arabia). The working distance was 15 mm with an accelerating voltage of 10 kV.

2.4. Simulation Details

2.4.1. Hirshfeld Surface Analysis

The Crystal Explorer 3.1 program (Perth, Australia) was used to create the Hirshfeld molecular surfaces and their relative two-dimensional (2D) fingerprint plots [32,33]. The normalized contact distance d_{norm} [34] based on Bondi's van der Waals radii [35] and 2D fingerprint plots were used for quantifying and decoding the inter-contacts in the crystal packing. The intense red color arises as a

result of contacts shorter than the sum of van der Waals radii, which are indicated by negative values of d_{norm} . The other intermolecular distances close to van der Waals contacts, with d_{norm} equal to zero, appear as light-red spots. In turn, contacts with positive d_{norm} values which are longer than the sum of van der Waals radii are colored with blue. Furthermore, d_e (inside) and d_i (outside) represent the distance from the point to the nearest nucleus external and internal to the surface with respect to the relative van der Waals radii. The intermolecular interactions in the crystal are summarized by the combination of d_e and d_i in the form of a 2D fingerprint plot.

The enrichment ratio E_{XY} for a pair of elements (X, Y) is defined as the ratio between the proportion of actual contacts in the crystal (C_{XY}) and the theoretical proportion of equi-distributed random contacts R_{XY} [36].

$$E_{XY} = C_{XY}/R_{XY}$$

A pair of elements has a high tendency to form contacts in the crystal if their enrichment ratio is larger than unity, while pairs which have an E value lower than unity tend to avoid contact with each other.

2.4.2. Computer Morphology Simulation

The crystal morphology predictions were created using a preliminary equilibration procedure, by means of the Forcite tools implemented in the Material Studio 7.0 package (San Diego, CA, USA) of Accelrys [37], assuming the molecular mechanics approximation and the Universal Force Field (UFF) [38]. The crystal structures used to simulate morphology were determined from the cif file containing all the crystallographic information. The morphology process was based on the Bravais–Friedel, Donnay–Harker (BFDH) and growth morphology (GM) methods. The minimum interplanar distance (d_{hkl}) for facet list generation was set to 1 Å, with a maximum value of 5 for the Miller indices and no limit for the overall number of growing facets. The crystal morphology simulation was achieved in vacuum and, consequently, it did not take into account any experimental conditions.

3. Results and Discussion

3.1. Energy-Dispersive X-ray Spectroscopy (SEM-EDX)

SEM image (Figure S1, Supplementary Materials) analysis shows that the surfaces of the hybrid appeared in the form of flat surfaces, which designates a good crystal quality. The EDX analysis associated with the SEM was carried out in zones of high contrast. The EDX measurements were conducted to confirm the presence of heavy element compositions of the crystal. They show the presence of characteristic carbon, iodine, bismuth, and oxygen signals.

3.2. Structure Description

The title compound $\text{Bi}_4\text{I}_{16} \cdot 4(\text{C}_6\text{H}_9\text{N}_2) 2(\text{H}_2\text{O})$ crystallizes in the monoclinic space group $P2_1/n$ (Table 1). Half of the $(\text{Bi}_4\text{I}_{16})^{4-}$ anion of the structure sits on a crystallographic inversion center; two 1-allylimidazolium cations $(\text{C}_6\text{H}_9\text{N}_2)^+$ and one water molecule complete the asymmetric unit (Figure 1). Each Bi(III) atom is six-coordinated by I atoms in a distorted octahedral geometry, and each BiI_6 octahedron is linked to another by two I atoms, forming a tetranuclear centrosymmetric cluster via edge-sharing. There are three types of I atoms: (i) I_4 and I_4^i [symmetry code: (i) $1 - x, 1 - y, 1 - z$] bridge three bismuth centers ($\mu_3\text{-I}$); (ii) I_2 , I_2^i [symmetry code: (i) $1 - x, 1 - y, 1 - z$], I_5 , and I_5^i bridge two bismuth centers ($\mu_2\text{-I}$); (iii) the remaining I atoms (I_1 , I_3 , I_5 , I_6 , I_7 , I_8) are terminally bonded to Bi atoms. The range of B–I bonds is 2.8898 (7)–3.3309 (6) Å, with a range of 3.3196 (6)–3.3309 (6) Å for bonds involving ($\mu_3\text{-I}$) atoms and 3.0228 (6)–3.1416 (6) Å for bonds involving ($\mu_2\text{-I}$) atoms. The bond angles I–Bi–I range between of 84.369 (15)° and 96.58 (3)°, suggest the high distortion of octahedra (Table 2). The shortest $\text{I}_6 \cdots \text{I}_7^{\text{ii}}$ [symmetry code: (ii) $x - 1/2, y - 3/2, z - 1/2$] distance is 3.8603(10) Å, which is shorter than the sum of van der Waals radii of two iodine atoms (4.3 Å) [39]. This indicates the presence of strong I⋯I interactions. All bond distances and angles of this cluster are in agreement with

the related iodobismuthate compounds [40–42]. The packing diagram for $\text{Bi}_4\text{I}_{16}\cdot 4(\text{C}_6\text{H}_9\text{N}_2)\cdot 2(\text{H}_2\text{O})$ is shown in Figure 2, where it is observed that the organic–inorganic (110) layers stack in a slightly offset ABAB manner. The supramolecular hydrogen-bonding patterns associated with both imidazolium groups of the $(\text{C}_6\text{H}_9\text{N}_2)^+$ cation in the title compound are shown in Figure 3. The terminal N–H moieties in $(\text{C}_6\text{H}_9\text{N}_2)^+$ cations act as hydrogen-bond donors with three iodine vertices of two isolated $(\text{Bi}_4\text{I}_{16})^{4-}$ anions via $\text{N}2\text{--H}2\text{N}\cdots\text{I}3$ and $\text{N}2\text{--H}2\text{N}\cdots\text{I}1$ interactions (Table 3). The water molecules connect the organic cations using $\text{N}4\text{--H}4\text{N}\cdots\text{O}1\text{W}$ hydrogen bonds, $\pi\text{--}\pi$ interactions with imidazolium rings, oxygen–centroid distances of 3.43 (1) Å, and oxygen–centroid of allyl group distances of 3.66 (1) Å. The organic cations are also interconnected by $\pi\text{--}\pi$ interactions between allyl groups and imidazolium rings (centroid allyl–centroid imidazolium ring distances of 4.03 (2) Å), as shown in Figure 4. Therefore, $\text{I}\cdots\text{I}$ interactions, hydrogen bonds, and $\pi\text{--}\pi$ interactions contribute to the structural stabilization.

Table 1. Crystallographic data and structure refinement parameters for $\text{Bi}_4\text{I}_{16}\cdot 4(\text{C}_6\text{H}_9\text{N}_2)\cdot 2(\text{H}_2\text{O})$.

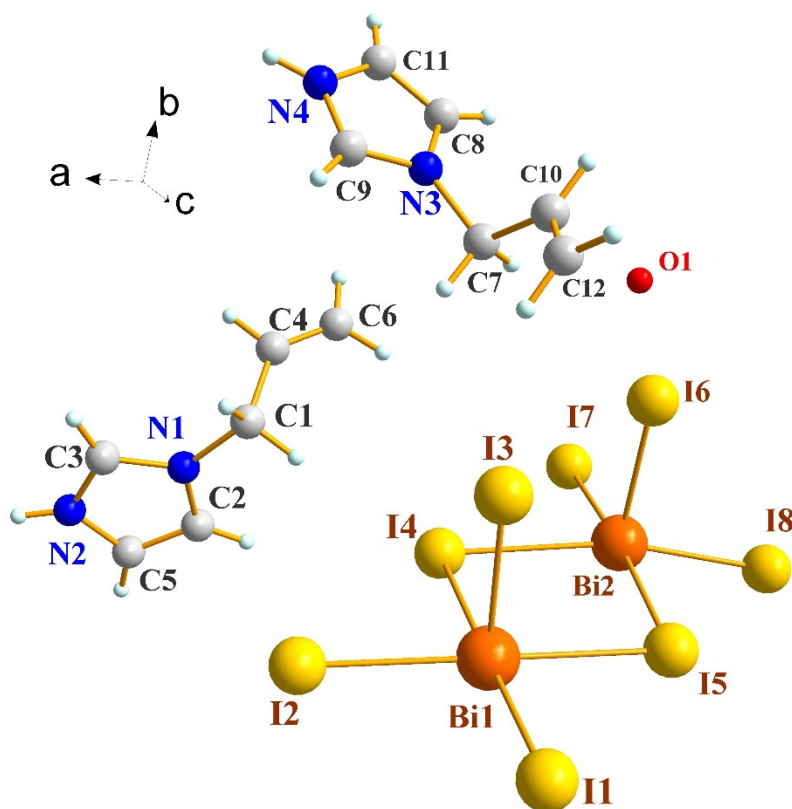
Empirical Formula	$\text{Bi}_4\text{I}_{16}\cdot 4(\text{C}_6\text{H}_9\text{N}_2)\cdot 2(\text{H}_2\text{O})$
Formula weight (g/mol)	3338.96
Crystal system, space group	Monoclinic, $P2_1/n$
a (Å)	11.312 (6)
b (Å)	25.985 (2)
c (Å)	11.879 (7)
β (°)	110.05 (2)
V (Å ³)	3280 (3)
Z	2
μ (mm ^{−1})	18.26
D_x (Mg·m ^{−3})	3.381
$F(000)$	3.381
Crystal size (mm)	$0.34 \times 0.33 \times 0.20$
Crystal habit	Block, orange
$\theta_{\text{min}}/\theta_{\text{max}}$ (°)	2.5/28.4
Measured reflections	113,427
Independent reflections	8177
Observed reflections with $I > 2\sigma(I)$	6751
R_{int}	0.116
Data/restraints/parameters	8177/0/245
$R[F^2 > 2\sigma(F^2)]$	0.042
$wR(F^2)$	0.091
Goof = S	1.086
$\Delta\rho_{\text{max}}/\Delta\rho_{\text{min}}$ (e Å ^{−3})	1.55/−1.39

Table 2. Selected bond distances and angles of $\text{Bi}_4\text{I}_{16}\cdot 4(\text{C}_6\text{H}_9\text{N}_2)\cdot 2(\text{H}_2\text{O})$.

Bond Distances (Å)			
Bi1–I3	2.9033 (6)	Bi2–I6	2.8918 (7)
Bi1–I1	2.9219 (6)	Bi2–I7	2.9581 (6)
Bi1–I2	3.0228 (6)	Bi2–I5	3.2456 (6)
Bi1–I5	3.1416 (6)	Bi2–I2 ⁱ	3.3271 (6)
Bi1–I4	3.3196 (6)	Bi2–I4	3.3418 (6)
Bi1–I4 ⁱ	3.3309 (6)	I2–Bi2 ⁱ	3.3272 (6)
Bi2–I8	2.8898 (7)	I4–Bi1 ⁱ	3.3308 (6)
Bond Angles (°)			
I3–Bi1–I1	92.74 (2)	I8–Bi2–I6	96.58 (3)
I3–Bi1–I2	89.82 (2)	I8–Bi2–I7	95.71 (2)
I1–Bi1–I2	94.571 (2)	I6–Bi2–I7	91.90 (2)
I3–Bi1–I5	93.38 (2)	I8–Bi2–I5	87.97 (2)
I1–Bi1–I5	90.259 (2)	I6–Bi2–I5	90.35 (2)
I2–Bi1–I5	174.073 (2)	I7–Bi2–I5	175.43 (2)

Table 2. Cont.

I3–Bi1–I4	90.346 (2)	I8–Bi2–I2 ⁱ	85.10 (2)
I1–Bi1–I4	176.274 (2)	I6–Bi2–I2 ⁱ	178.23 (2)
I2–Bi1–I4	87.516 (2)	I7–Bi2–I2 ⁱ	88.458 (2)
I5–Bi1–I4	87.479 (2)	I5–Bi2–I2 ⁱ	89.170 (2)
I3–Bi1–I4 ⁱ	174.67 (2)	I8–Bi2–I4	167.43 (2)
I1–Bi1–I4 ⁱ	92.564 (2)	I6–Bi2–I4	94.14 (2)
I2–Bi1–I4 ⁱ	89.226 (2)	I7–Bi2–I4	90.443 (2)
I5–Bi1–I4 ⁱ	87.124 (16)	I5–Bi2–I4	85.427 (2)
I4–Bi1–I4 ⁱ	84.369 (15)	I2i–Bi2–I4	84.122 (2)

Symmetry code: (i) $-x + 1, -y + 1, -z + 1$.Figure 1. The asymmetric unit of $\text{Bi}_4\text{I}_{16} \cdot 4(\text{C}_6\text{H}_9\text{N}_2) \cdot 2(\text{H}_2\text{O})$, showing the atomic numbering scheme.Table 3. Hydrogen bonds in $\text{Bi}_4\text{I}_{16} \cdot 4(\text{C}_6\text{H}_9\text{N}_2) \cdot 2(\text{H}_2\text{O})$.

H-Bonds	D–H	H···A (Å)	D···A (Å)	$\angle(\text{DH}\cdots\text{A})$ (°)
N4–H4···O1W	0.86	1.96	2.79 (2)	162
N2–H2N···I1	0.86	3.42 (6)	3.89 (1)	126
N2–H2N···I3	0.86	3.48 (8)	3.97 (1)	125

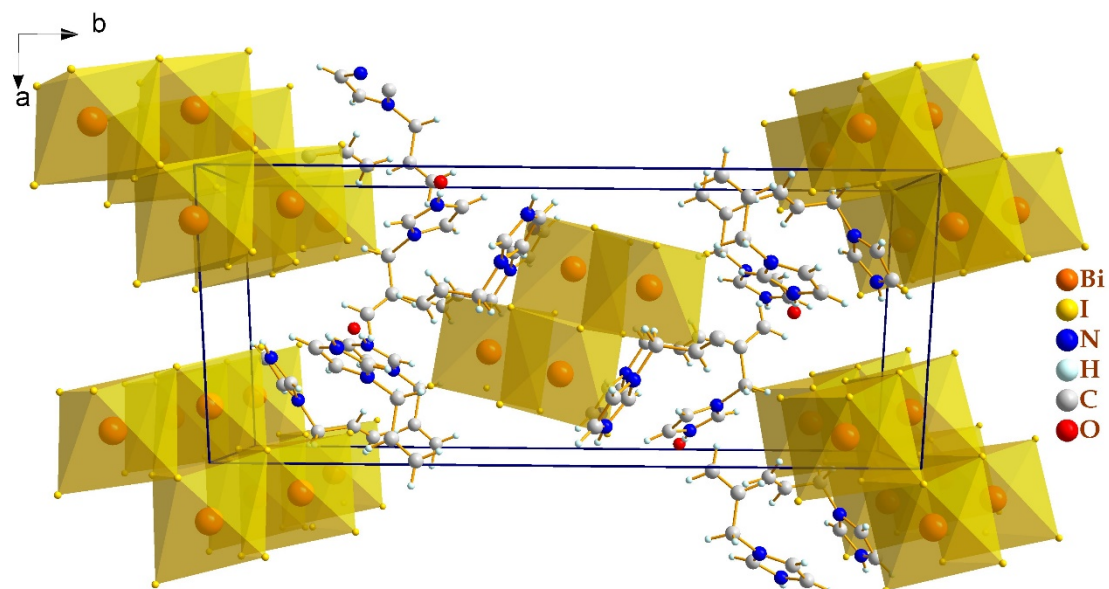


Figure 2. The (110) view of the crystal packing in $\text{Bi}_4\text{I}_{16}\cdot 4(\text{C}_6\text{H}_9\text{N}_2)\cdot 2(\text{H}_2\text{O})$.

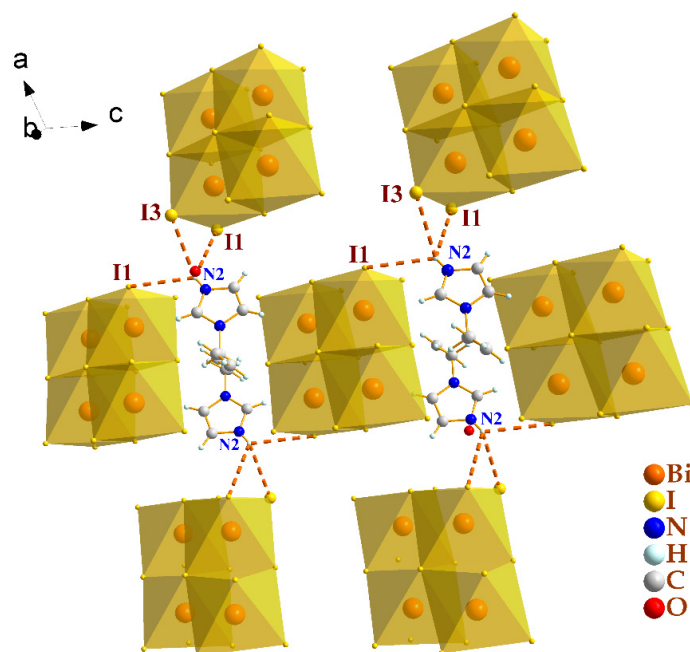


Figure 3. The hydrogen-bonding scheme of $\text{Bi}_4\text{I}_{16}\cdot 4(\text{C}_6\text{H}_9\text{N}_2)\cdot 2(\text{H}_2\text{O})$.

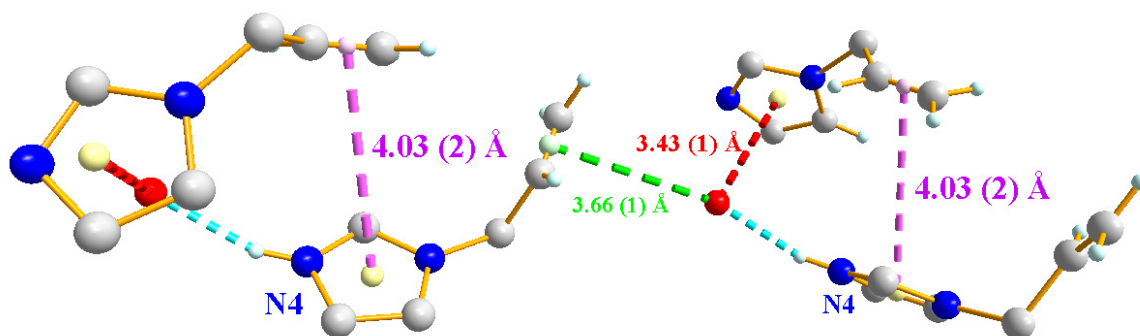


Figure 4. The π - π interactions between organic cations and water molecules in $\text{Bi}_4\text{I}_{16}\cdot 4(\text{C}_6\text{H}_9\text{N}_2)\cdot 2(\text{H}_2\text{O})$.

3.3. Hirshfeld Surface Analysis

The nature of intermolecular interactions in $\text{Bi}_4\text{I}_{16}\cdot 4(\text{C}_6\text{H}_9\text{N}_2) \cdot 2(\text{H}_2\text{O})$ was clarified using three-dimensional Hirshfeld surface analysis. The 2D fingerprint plots quantitatively revealed the contribution of those interactions in the crystal structure, presenting the surfaces that were mapped over a d_{norm} range of -0.614 to 1.100 , d_e range of 0.737 to 3.166 , and d_i range of 0.737 to 3.062 (Figure 5). The information of these surfaces is summarized in Table 3. The deep-red regions visible on the views of the d_{norm} surfaces represent hydrogen-bonding contacts: $\text{H}\cdots\text{I}$ and $\text{H}\cdots\text{O}$. The bright-red regions on the d_e surface focus on the hydrogen bond acceptor $\text{I}\cdots\text{H}$, where d_e is short, but the hydrogen bond donor $\text{H}\cdots\text{I}$ is observed as the red area of the d_i surface (Figure 5). The greatest contribution from the $\text{I}\cdots\text{H}/\text{H}\cdots\text{I}$ contacts is 56.3%, corresponding to $\text{N}-\text{H}\cdots\text{I}$ interactions, as illustrated by a pair of sharp spikes characteristic of strong hydrogen-bonding interactions in the 2D fingerprint plot (Figure 6). There are actually two $\text{N}_2-\text{H}_2\text{N}\cdots\text{I}_1$ and $\text{N}_2-\text{H}_2\text{N}\cdots\text{I}_3$ hydrogen bonds in the crystal structure (Table 3). Furthermore, these types of contacts are the most common interactions due to the abundance of iodine and hydrogen on the molecular surface ($\% S_{\text{I}} = 39.7\%$ and $\% S_{\text{H}} = 45.6\%$) and an enrichment ratio higher than the unit $E_{\text{H}\cdots\text{I}} = 1.55$ (Table 4). In addition, the $\text{H}\cdots\text{H}$ interactions appear as a large region of the 2D fingerprint plot with a high concentration in the middle region, comprising 11.7% of the total Hirshfeld surface area (Figure 6); they are the second most frequent interactions due to the richness of hydrogen on the molecular surface (45.6%). The $\text{H}\cdots\text{O}$ contacts, which refer to $\text{N}-\text{H}\cdots\text{O}$ interactions, represent the third most important interaction on the surface with a percentage around 8.1% of the Hirshfeld surfaces (Figure 6) and an enrichment ratio higher than unit $E_{\text{H}\cdots\text{O}} = 1.39$ (Table 4).

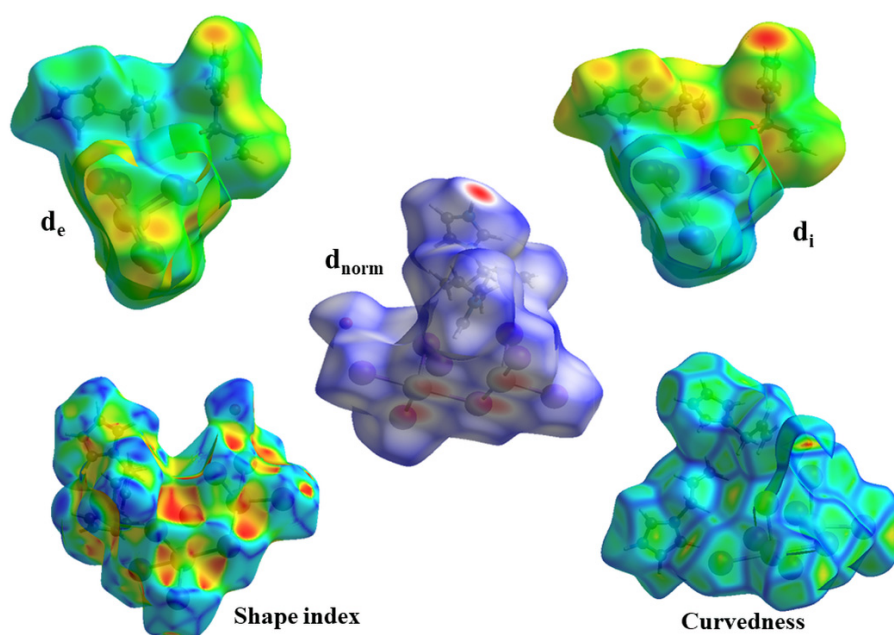


Figure 5. d_{norm} mapped on Hirshfeld surfaces for visualizing the intermolecular interactions, d_e , d_i , curvedness, and shape-index of $\text{Bi}_4\text{I}_{16}\cdot 4(\text{C}_6\text{H}_9\text{N}_2) \cdot 2(\text{H}_2\text{O})$.

Shape index and curvedness surfaces, illustrated in Figure 5, were used to discover planar stacking ($\pi\cdots\pi$) interaction arrangements. In the same region of the shape index surface, the presence of red and blue triangles in Figure 5 indicates that the $\pi\cdots\pi$ interactions are identically present in the crystal structure. Blue triangles represent the convex region which is formed due to the carbon and nitrogen atoms present in the molecule inside the surface, while red triangles having concave regions are due to the carbon atoms of π -stacked molecule above it. The mapping of curvedness on the Hirshfeld surface Figure 5 shows flat green regions separated by blue edges. The clearly visible flat regions on the curvedness surface are another characteristic of the $\pi\cdots\pi$ stacking interaction. The contribution of $\pi\cdots\pi$ stacking interactions ($\text{O}\cdots\text{C}$ and $\text{C}\cdots\text{C}$) was also investigated by Hirshfeld surfaces, as shown

in Figure 7. The O...C contacts contribute 1.7% to the total Hirshfeld surface area, which is a small percentage. The C...C contacts are a rare 0.3% of the total Hirshfeld surface area, but more enriched at $E_{C...C} = 1.87$ due to stacking between imidazole rings and allyl groups. The H...H interactions are reflected in the distribution of scattered points in the 2D fingerprint plot, which have a relatively significant contribution of 11.7% to the total Hirshfeld surface area of the molecules, but these contacts are slightly under-represented with an enrichment ratio around 0.56. The Hirshfeld surfaces of the bismuth atom in the compound, which were mapped over the d_{norm} surface, show deep-red regions for Bi, highlighting the short Bi...I and I...I contacts. The Bi...I and I...I contacts contribute 5.5% and 5.9% of the Hirshfeld surfaces, respectively. Thus, the Hirshfeld surface analysis adequately confirms the presence of the I...I interaction discussed in the structural description. Figure 7 presents the relative percentage contributions to the overall Hirshfeld surface. In conclusion, the Hirshfeld surface analysis elucidates the same results as the X-ray crystal structure analysis and explains the intermolecular interactions in a new visual manner.

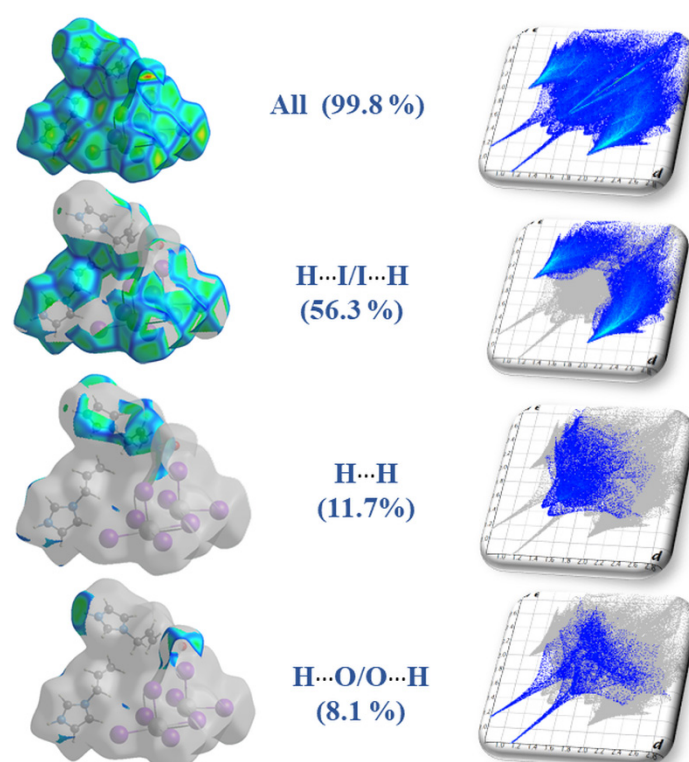


Figure 6. Fingerprint plots with d_{norm} view of H...I, H...H, and H...O contacts in $\text{Bi}_4\text{I}_{16}\cdot 4(\text{C}_6\text{H}_9\text{N}_2)\cdot 2(\text{H}_2\text{O})$.

Table 4. Hirshfeld contact surfaces and enrichment ratios for $\text{Bi}_4\text{I}_{16}\cdot 4(\text{C}_6\text{H}_9\text{N}_2)\cdot 2(\text{H}_2\text{O})$.

Atoms	H	C	N	O	I	Bi
Surface %	45.6	4	1.75	6.2	39.7	2.75
H	0.56	-	-	-	-	-
C	0.74	1.87	-	-	-	-
N	0.24	-	0.00	-	-	-
O	1.39	-	-	0.00	-	-
I	1.55	0.69	-	0.64	0.37	-
Bi	0.00	0.00	0.00	0.00	-	0.00

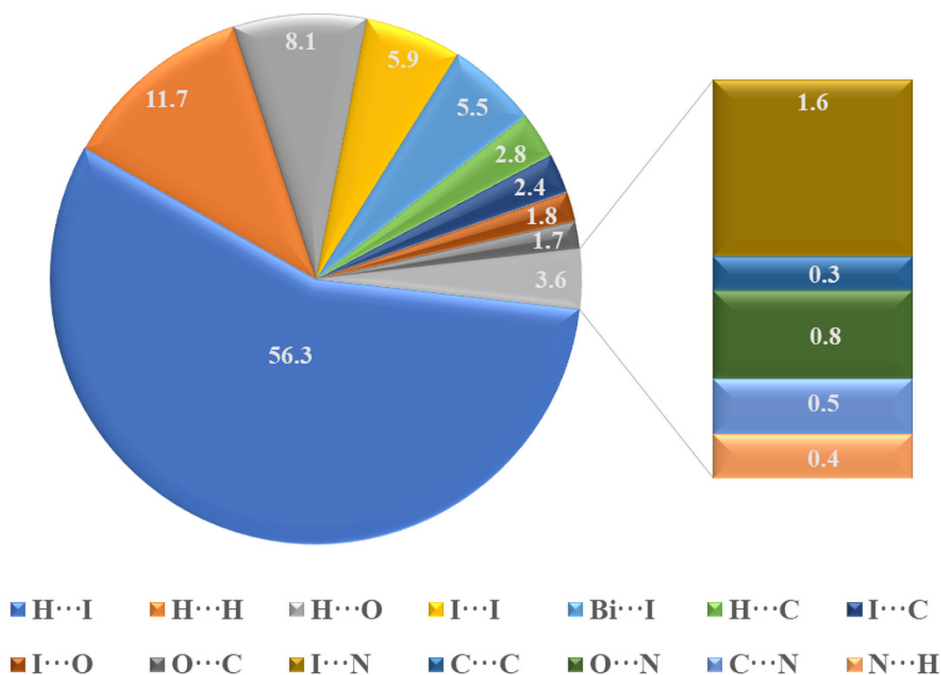


Figure 7. Relative contributions of different intermolecular contacts to the Hirshfeld surface area in $\text{Bi}_4\text{I}_{16}\cdot 4(\text{C}_6\text{H}_9\text{N}_2) 2(\text{H}_2\text{O})$.

3.4. Prediction of Crystal Morphology

Figure 8 shows that there is an extraordinary similarity between the simulated crystal morphology based on BFDH and growth morphology (GM) methods (Figure 8b,c) and the experimental one (Figure 8a) assessed by scanning electronic microscopy (SEM).

The vacuum morphology of $\text{Bi}_4\text{I}_{16}\cdot 4(\text{C}_6\text{H}_9\text{N}_2) 2(\text{H}_2\text{O})$ was generated by the BFDH model (Figure 8b), which gave five important facets along with their planes (hkl), center-to-plane distance (d_{hkl}), and % surface area. The BFDH method is an approximation where facet growth rates are assumed to be inversely proportional to the interplanar spacings d_{hkl} in the lattice [43]. Table 5 lists the inter-planar spacings of various low index facets of the crystal habit of the title compound based on the BFDH calculation. It shows that the crystal facets are made up by (020), (011), (110), (10–1), and (11–1) planes, of which (020) with 28.84% of the total facet area was the most important facet. The calculated aspect ratio by BFDH morphology was 1.713. In the second step, morphology was determined by the GM method, which shows (Table 5 and Figure 8c) that the crystal facets are dominated by (020), (011), (110), (10–1), and (11–1) planes, of which (020) with 30.77% and (10–1) with 27.26% of total facet area were the most important facets. The calculated aspect ratio for the GM model was 1.88. Figure 9 show the result analysis of morphology prediction by the GM method, illustrating the hkl plane corresponding to the morphological important crystal facets described in the habit, while simply taking into account which types of groups are extended from the considered facet. It is evident that the (020) and (10–1) morphological importance facets, which represent more than the 57% of the crystal surface, are occupied by a small number of polar groups (small interactions). The attachment energies of (020) and (10–1) are -32.0392 and -33.1538 $\text{kJ}\cdot\text{mol}^{-1}$, respectively. The other morphological important facets demonstrate the presence of polar functional groups (stronger interactions). The attachment energy calculations were performed to explain the probable energetic interactions during crystal growth. If the attachment energy is the lowest in a particular direction, the morphologically important facet bounding that growth direction has the slowest growth rate and will be the smallest [44]. According to the E_{att} value, the (11–1) and (011) facets present the stronger interaction and their growth rates are also faster than that of the (020), (10–1), and (110) facets.

Table 5. Morphology predictions for $\text{Bi}_4\text{I}_{16}\cdot 4(\text{C}_6\text{H}_9\text{N}_2)\cdot 2(\text{H}_2\text{O})$ through Bravais–Friedel, Donnay–Harker (BFDH) (upper) and growth morphology (GM) (lower) calculations. The percentage of total facet area (TFA) is calculated as $100 \times (\text{hkl facet area})/(\text{total surface area})$.

BFDH				
hkl	Multiplicity	D_{hkl} (Å)	% of TFA	
(0 2 0)	2	12.99	28.84	
(0 1 1)	4	10.25	28.64	
(1 1 0)	4	9.84	25.60	
(1 0 $\bar{1}$)	2	9.49	9.73	
(1 1 $\bar{1}$)	4	8.92	7.19	
Growth Morphology				
hkl	Multiplicity	d_{hkl} (Å)	E_{att} (Total) (kcal·mol $^{-1}$)	% of TFA
(0 2 0)	2	12.99	−32.0392	30.77
(1 0 $\bar{1}$)	2	9.49	−33.1538	27.26
(1 1 0)	4	9.84	−39.0501	20.81
(0 1 1)	4	10.25	−51.9067	13.96
(1 1 $\bar{1}$)	4	8.91	−58,9835	7.10

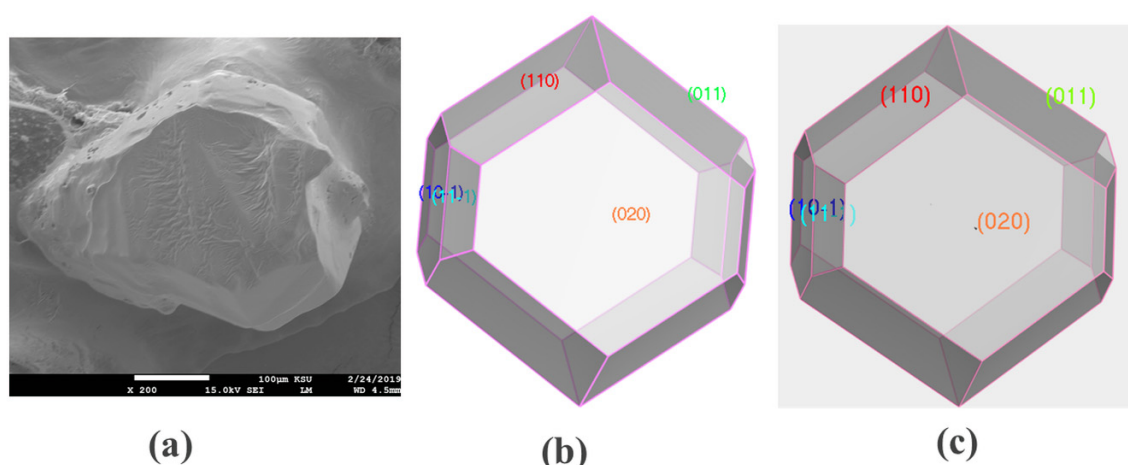


Figure 8. Crystal morphology comparison between the SEM images (a); BFDH model (b); GM model (c). The morphologically important (MI) facets are presented by their Miller indices.

3.5. Infrared (IR) and Raman Spectroscopy

IR and Raman spectroscopy were completed to give information on the molecular interactions existing in $\text{Bi}_4\text{I}_{16}\cdot 4(\text{C}_6\text{H}_9\text{N}_2)\cdot 2(\text{H}_2\text{O})$. The tentative assignment of the internal vibrations of the allylimidazolium cations is based on the previously reported vibrational studies on materials containing the allylimidazolium cation [45]. The assignments of the internal vibrations of the $(\text{Bi}_4\text{I}_{16})^{4-}$ anions are proposed on the basis of the results obtained for numerous halogenobismuthate (III) derivatives [46–49].

The Raman spectrum (Figure 10) recorded in the 50–400 cm^{-1} frequency range showed six bands at 63 cm^{-1} , 94 cm^{-1} , 80 cm^{-1} , 108 cm^{-1} , 124 cm^{-1} and 144 cm^{-1} associated with the inorganic cluster. The strong Raman line at 144 cm^{-1} clearly corresponds to the symmetric Bi–I stretching mode of the external iodides. In turn, the feeble Raman line near 124 cm^{-1} is due to the asymmetric Bi–I stretching mode. The stretching modes for the bridged I–Bi–I give a weak Raman line at 108 cm^{-1} . The additional weak bands visible at 63 cm^{-1} , 94 cm^{-1} and 80 cm^{-1} may be assigned to the bending modes of the external iodides and the bridged I–Bi–I.

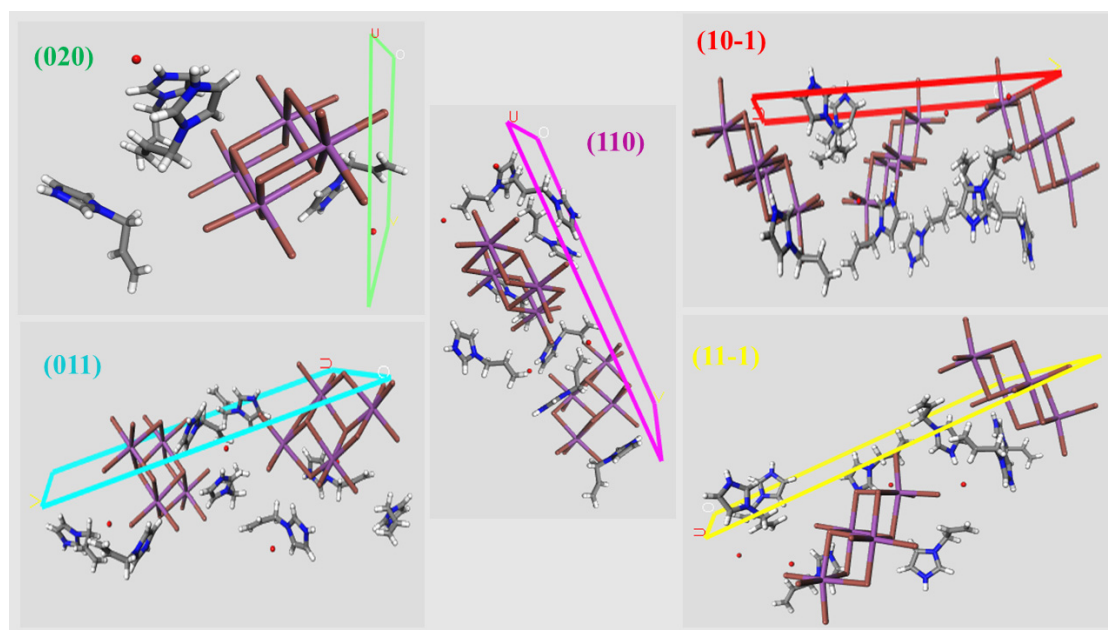


Figure 9. Cleavage structure of main exposure crystal planes of $\text{Bi}_4\text{I}_{16}\cdot 4(\text{C}_6\text{H}_9\text{N}_2)\cdot 2(\text{H}_2\text{O})$ indicating the presence of different functional groups.

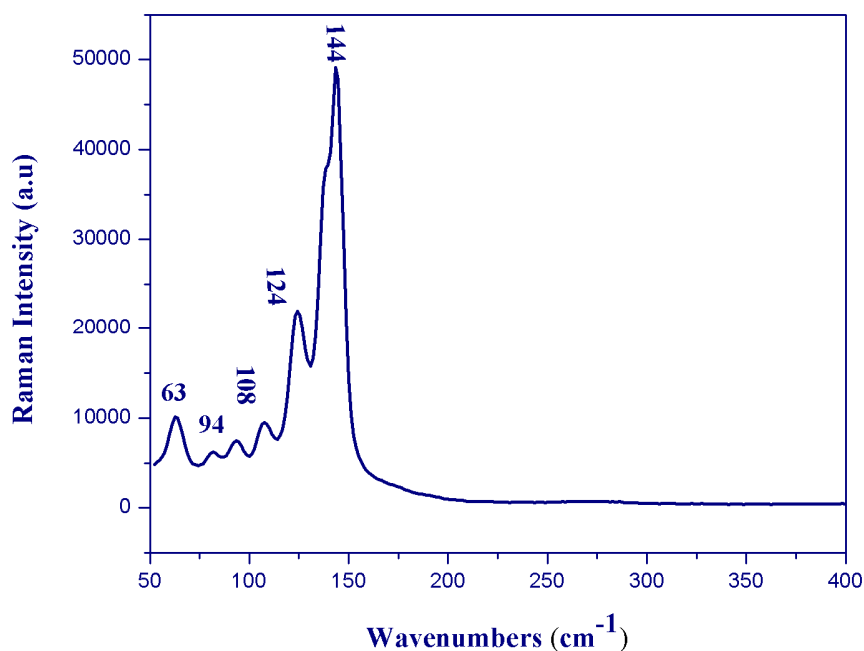


Figure 10. Raman spectrum of $\text{Bi}_4\text{I}_{16}\cdot 4(\text{C}_6\text{H}_9\text{N}_2)\cdot 2(\text{H}_2\text{O})$.

The infrared spectrum (Figure 11) recorded between 400 and 4000 cm^{-1} shows, at high wavenumbers, an absorption at 3546 cm^{-1} assignable to N–H stretching modes. The weak bands between 2924 and 2824 cm^{-1} are assigned to (C–H) stretching modes. The peaks observed at 1623 and 1265 cm^{-1} correspond to stretching vibrations of (C=N) and (C–N) bonds, respectively. C=C and C–C stretching vibrations are observed at 1402 cm^{-1} and 1046 cm^{-1} , respectively. The bands corresponding to the deformation (CC) and (CN) groups appeared in the 996 – 800 cm^{-1} range. The vibrations at 736 cm^{-1} and 612 cm^{-1} were due to the deformation (C–H) of the imidazolium group. Finally, the bands at 550 cm^{-1} and 439 cm^{-1} were associated with the rocking and wagging vibrations of C–H and N–H bands.

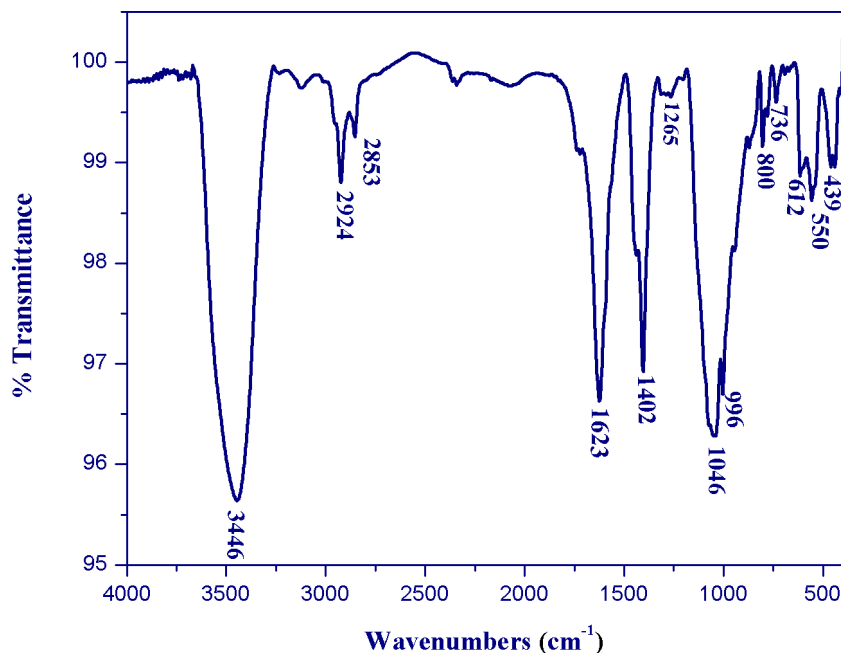


Figure 11. Vibrational spectrum of $\text{Bi}_4\text{I}_{16}\cdot 4(\text{C}_6\text{H}_9\text{N}_2)\cdot 2(\text{H}_2\text{O})$.

4. Conclusions

The crystal structure of the new organic–inorganic material $\text{Bi}_4\text{I}_{16}\cdot 4(\text{C}_6\text{H}_9\text{N}_2)\cdot 2(\text{H}_2\text{O})$ was determined. This compound crystallizes in the monoclinic system at room temperature. The crystal structure is formed by an alternation of organic and inorganic entities linked via hydrogen bonds developing a three-dimensional structure. The Hirshfeld surface analysis of the crystal structure clarifies that the most important contribution for crystal packing is from $\text{H}\cdots\text{I}$ (56.3%) and $\text{H}\cdots\text{H}$ (11.7%) interactions and confirms the presence of $\text{I}\cdots\text{I}$ interactions between inorganic clusters. The predicted morphology was compared with the results based on BFDH and GM models and with the experimentally observed morphology. The main crystal facets (002), (101), (011), and (012) were observed to be dominant in the morphology predicted by the two models. By cleaving these dominant crystal facets, surface chemistry visualization and theoretical analysis based on the presence of polar groups (H-band interactions) for the important morphological forms were achieved. Finally, the experimental IR and Raman spectra allowed us to assign the vibration modes present in the title compound.

Supplementary Materials: The following are available online at <http://www.mdpi.com/2073-4352/10/5/397/s1>, Figure S1. SEM image, EDS spectrum and qualitative results of $\text{Bi}_4\text{I}_{16}\cdot 4(\text{C}_6\text{H}_9\text{N}_2)\cdot 2(\text{H}_2\text{O})$ single crystal; Table S1. Fractional atomic coordinates and isotropic or equivalent isotropic displacement parameters (\AA^2). CCDC-1908070 contains the supplementary crystallographic data for $\text{Bi}_4\text{I}_{16}\cdot 4(\text{C}_6\text{H}_9\text{N}_2)\cdot 2(\text{H}_2\text{O})$. These data can be obtained free of charge from The Cambridge Crystallographic Data Center via http://www.ccdc.cam.ac.uk/data_request/cif.

Funding: This research received no external funding.

Conflicts of Interest: The authors declare no conflict of interest.

References

1. Ali, S.B.; Ferretti, V.; Bianco, L.D.; Spizzo, F.; Belhouchet, M. Structural, vibrational, optical properties and theoretical studies of a new organic inorganic material: Tris-acetoguanaminium hexachlorobismuthate monohydrate. *J. Mol. Struct.* **2020**, *1199*, 126986. [[CrossRef](#)]
2. Zhang, R.; Mao, X.; Yang, Y.; Yang, S.; Zhao, W.; Wumaier, T.; Wei, D.; Deng, W.; Han, K. Air-Stable, Lead-Free Zero-Dimensional Mixed Bismuth-Antimony Perovskite Single Crystals with Ultrabroad Band Emission. *Angew. Chem. Int. Ed.* **2019**. [[CrossRef](#)]
3. Wei, Y.; Cheng, Z.; Lin, J. An overview on enhancing the stability of lead halide perovskite quantum dots and their applications in phosphor-converted LEDs. *Chem. Soc. Rev.* **2019**, *48*, 310. [[CrossRef](#)] [[PubMed](#)]

4. Szklarz, P.; Jakubas, R.; Piecha-Bisiorek, A.; Bator, G.; Chanski, M.; Medycki, W.; Wuttke, J. Organic-inorganic hybrid crystals, (2,4,6-CH₃PyH)₃Sb₂Cl₉ and (2,4,6-CH₃PyH)₃Bi₂Cl₉. Crystal structure characterization and tunneling of CH₃ groups studied by ¹H NMR and neutron spectroscopy. *Polyhedron* **2018**, *139*, 249–256. [[CrossRef](#)]
5. Igbari, F.; Wang, Z.K.; Liao, L.S. Progress of Lead-Free Halide Double Perovskites. *Adv. Energy Mater.* **2019**, 1803150. [[CrossRef](#)]
6. Zhou, C.; Lin, H.; Neu, J.; Zhou, Y.; Chaaban, M.; Lee, S.; Worku, M.; Chen, B.; Clark, R.J.; Cheng, W.; et al. Green Emitting Single-Crystalline Bulk Assembly of Metal Halide Clusters with NearUnity Photoluminescence Quantum Efficiency. *ACS Energy Lett.* **2019**, *4*, 1579–1583. [[CrossRef](#)]
7. Ahern, J.C.; Nicholas, A.D.; Kelly, A.W.; Chan, B.; Pike, R.D.; Patterson, H.H. A terbium chlorobismuthate(III) double salt: Synthesis, structure, and photophysical properties. *Inorg. Chim. Acta* **2018**, *478*, 71–76. [[CrossRef](#)]
8. AKelly, W.; Nicholas, A.; Ahern, J.C.; Chan, B.; Patterson, H.H.; Pike, R.D. Alkali metal bismuth (III) chloride double salts. *J. Alloy. Compd.* **2016**, *670*, 337–345. [[CrossRef](#)]
9. Sorg, J.R.; Wehner, T.; Matthes, P.R.; Sure, R.; Grimme, S.; Heine, J.K. Müller- Buschbaum. Bismuth as a versatile cation for luminescence in coordination polymers from BiX₃/4,4'-bipy: Understanding of photophysics by quantum chemical calculations and structural parallels to lanthanides. *Dalton. Trans.* **2018**, *47*, 7669–7681. [[CrossRef](#)] [[PubMed](#)]
10. Wagner, B.; Dehnhardt, N.; Schmid, M.; Klein, B.P.; Ruppenthal, L.; Müller, P.; Zugermeier, M.; Gottfried, J.M.; Lippert, S.; Halbich, M.U.; et al. Color change effect in an organic-inorganic hybrid material based on a porphyrin diacid. *J. Phys. Chem. C* **2016**, *120*, 28363–28373. [[CrossRef](#)]
11. Frolova, L.A.; Anokhin, D.V.; Piryazev, A.A.; Luchkin, S.Y.; Dremova, N.N.; Troshin, P.A. Highly Efficient All-Inorganic Planar Heterojunction Perovskite Solar Cells Produced by Thermal Coevaporation of CsI and PbI₂. *J. Phys. Chem. Lett.* **2017**, *8*, 67–72. [[CrossRef](#)] [[PubMed](#)]
12. Fabian, D.M.; Ardo, S. Hybrid organic-inorganic solar cells based on bismuth iodide and 1,6-hexanediammonium dication. *J. Mater. Chem. A* **2016**, *4*, 6837–6841. [[CrossRef](#)]
13. Sichert, J.A.; Hemmerling, A.; Daw, C.C.; Urban, A.S.; Feldmann, J. Tuning the optical bandgap in layered hybrid perovskites through variation of alkyl chain length. *APL Mater.* **2019**, *7*, 041116. [[CrossRef](#)]
14. Ganose, A.M.; Savory, C.N.; Scanlon, D.O. Beyond methylammonium lead iodide: Prospects for the emergent field of ns² containing solar absorbers. *Chem. Commun.* **2017**, *53*, 20. [[CrossRef](#)] [[PubMed](#)]
15. Adonin, S.A.; Sokolov, M.N.; Fedin, V.P. Polynuclear halide complexes of Bi(III): From structural diversity to the new properties. *Coord. Chem. Rev.* **2016**, *312*, 1–21. [[CrossRef](#)]
16. Adonin, S.A.; Gorokh, I.D.; Novikov, A.S.; Samsonenko, D.G.; Yushina, I.V.; Sokolov, M.N.; Fedin, V.P. Halobismuthates with halopyridinium cations: Appearance or non-appearance of unusual colouring. *Cryst. Eng. Commun.* **2018**, *20*, 776. [[CrossRef](#)]
17. Adonin, S.A.; Usoltsev, A.N.; Novikov, A.S.; Kolesov, B.A.; Fedin, V.P.; Sokolov, M.N. One- and Two-Dimensional Iodine-Rich Iodobismuthate(III) Complexes: Structure, Optical Properties, and Features of Halogen Bonding in the Solid State. *Inorg. Chem.* **2020**, *59*, 3290–3296. [[CrossRef](#)]
18. Adonin, S.A.; Sokolov, M.N.; Fedin, V.P. Bismuth(III) Halide Complexes: New Structural Types and New Application Areas. *Russ. J. Inorg. Chem.* **2017**, *62*, 1789–1796. [[CrossRef](#)]
19. AUsoltsev, N.; Elshobaki, M.; Adonin, S.A.; Frolova, L.A.; Derzhavskaya, T.; Abramov, P.A.; Anokhin, D.V.; Korolkov, I.V.; Luchkin, S.Y.; Dremova, N.N.; et al. Polymeric iodobismuthates {[Bi₃I₁₀]} and {[BiI₄]} with N-heterocyclic cations: Promising perovskite-like photoactive materials for electronic devices. *J. Mater. Chem. A* **2019**, *7*, 5957–5966. [[CrossRef](#)]
20. Attia, S.; Chaari, N.; Chaabouni, S. Synthesis, Crystal Structure, and Dielectric Properties of (3-Aminopropyl-imidazolium) Pentachlorobismuthate(III) [C₆H₁₃N₃]BiCl₅. *J. Cluster. Sci.* **2015**. [[CrossRef](#)]
21. Sharutin, V.V.; Yegorova, I.V.; Klepikov, N.N.; Boyarkina, E.A.; Sharutin, O.K. Synthesis and structure of bismuth complexes [Ph₃MeP]⁶⁺[BiI₃Br₃]³⁻[Bi₂I₆Br₃]³⁻·H₂O₂, [Ph₃EtP]³⁺[Bi₂I₉]³⁻, n[Ph₃MeP]³⁺[Bi₃I₁₂]³⁻, [Ph₃(iso-Pr)P]³⁺[Bi₃I₁₂]³⁻·2Me₂C=O, and [Ph₄Bi]³⁺[Bi₅I₁₈]³⁻. *Russ. J. Inorg. Chem.* **2009**, *54*, 52. [[CrossRef](#)]
22. Yelovik, N.A.; Shestimerov, T.A.; Bykov, M.A.; Wei, Z.; Dikarev, E.V.; Shevelkov, A.V. Synthesis, structure, and properties of LnBiI₆·13H₂O (Ln = La, Nd). *Russ. Chem. Bull.* **2017**, *66*, 1196. [[CrossRef](#)]
23. Krautscheid, H. Synthese und Kristallstrukturen von (Ph₄P)₄[Bi₈I₂₈], (nBu₄N)[Bi₂I₇] und (Et₃PhN)₂[Bi₃I₁₁]⁻ Iodobismutate mit isolierten bzw polymeren Anionen. *Z. Anorg. Allg. Chem.* **1995**, *621*, 2049. [[CrossRef](#)]
24. Buikin, P.A.; Rudenko, A.Y.; Baranchikov, A.E.; Ilyukhin, A.B.; Kotov, V.Y. 1D-Bromobismuthates of Dipyrindinoalkane Derivatives. *Russ. J. Coord. Chem.* **2018**, *44*, 373–379. [[CrossRef](#)]

25. Shestimerova, T.A.; Yelavik, N.A.; Mironov, A.V.; Kuznetsov, A.N.; Bykov, M.A.; Grigorieva, A.V.; Utochnikova, V.V.; Lepnev, L.S.; Shevelkov, A.V. From Isolated Anions to Polymer Structures through Linking with I₂: Synthesis, Structure, and Properties of Two Complex Bismuth(III) Iodine Iodides. *Inorg. Chem.* **2018**, *57*, 4077. [[CrossRef](#)] [[PubMed](#)]
26. Zhang, Z.P.; Feng, Q.Y.; Wang, Q.L.; Huang, X.; Chen, D.; Zhou, J. A New Iodobismuthate-Based Hybrid Containing Mixed Iodobismuthate Clusters Templated by Diammonium Cation: Structure and Photocurrent Response. *J. Cluster. Sci.* **2018**, *29*, 367. [[CrossRef](#)]
27. Bruker APEX3; Bruker AXS Inc.: Madison, WI, USA, 2017.
28. Bruker SAINT; Bruker AXS Inc.: Madison, WI, USA, 2017.
29. Sheldrick, G.M. SADABS Bruker; AXS Inc.: Madison, WI, USA, 2017.
30. Sheldrick, G.M. Crystal structure refinement with SHELXL. *Acta Cryst.* **2015**, *C71*, 3–8.
31. Brandenburg, K. DIAMOND; Crystal Impact GbR: Bonn, Germany, 2008.
32. Wolff, S.K.; Grimwood, D.J.; McKinnon, J.J.; Turner, M.J.; Jayatilaka, D.; Spackman, M.A. *Crystal Explorer (Version 3.1)*; University of Western: Perth, Australia, 2012.
33. Spackman, M.A.; Jayatilaka, D. Hirshfeld surface analysis. *CrystEngComm* **2009**, *11*, 19. [[CrossRef](#)]
34. McKinnon, J.J.; Jayatilaka, D.; Spackman, M.A. Towards quantitative analysis of intermolecular interactions with Hirshfeld surfaces. *Chem. Commun.* **2007**, *37*, 3814–3816. [[CrossRef](#)]
35. Bondi, A. Van der Waals Volumes and Radii of Metals in Covalent Compounds. *J. Phys. Chem.* **1966**, *70*, 3006–3007. [[CrossRef](#)]
36. Jelsch, C.; Ejsmont, K.; Huder, L. The enrichment ratio of atomic contacts in crystals, an indicator derived from the Hirshfeld surface analysis. *IUCrJ* **2014**, *1*, 119–128. [[CrossRef](#)] [[PubMed](#)]
37. *Materials Studio, Version 7.0*; Accelrys Software Inc.: San Diego, CA, USA, 2013.
38. Rappe, A.K.; Casewit, C.J.; Colwell, K.S.; Goddard, W.A., III; Skiff, W.M. UFF, a full periodic table force field for molecular mechanics and molecular dynamics simulations. *J. Am. Chem. Soc.* **1992**, *114*, 10024–10035. [[CrossRef](#)]
39. Goforth, A.M.; Gardinier, J.R.; Smith, M.D.; Peterson, L.R.; Loye, H.C.Z. [Ru(2,2'-bipy)3]2[Bi4I 16]: A bimetallic inorganic-organic complex consisting of a d-metal coordination cation and a polynuclear iodobismuthate anion. *Inorg. Chem. Commun.* **2005**, *8*, 684–688. [[CrossRef](#)]
40. Carmalt, C.J.; Farrugia, L.J.; Norman, N.C. Synthesis and X-ray Crystal Structure of a Polymeric Iodobismuthate Anion. *Z. Naturforsch. B* **1995**, *50*, 1591–1596. [[CrossRef](#)]
41. Kubiak, R.; Ejsmont, K. Crystal structure of a novel bismuth phthalocyanine-bismuth iodide complex. *J. Mol. Struct.* **1999**, *474*, 275–281. [[CrossRef](#)]
42. Bondi, A.J. van der Waals Volumes and Radii. *J. Phys. Chem.* **1964**, *68*, 441–451. [[CrossRef](#)]
43. GDestri, L.; Marrazzo, A.; Rescifina, A.; Punzo, F. Crystal Morphologies and Polymorphs in Tolbutamide Microcrystalline Powder. *J. Pharm. Sci.* **2013**, *102*, 73–83. [[CrossRef](#)] [[PubMed](#)]
44. Hartman, P.; Bennema, P. The attachment energy as a habit controlling factor: I. Theoretical considerations. *J. Cryst. Growth.* **1980**, *49*, 145–156. [[CrossRef](#)]
45. Piecha, A.; Jakubas, R.; Pietraszko, A. Phase transitions and electric properties of imidazolium chlorobismuthate(III): [C₃H₅N₂]₆[Bi₄Cl₁₈]. *J. Mol. Struct.* **2007**, *829*, 149. [[CrossRef](#)]
46. Belkhal, I.; Mokhlisse, R.; Tanouti, B.; Chanh, N.B.; Couzi, M. X-ray Diffraction and Raman Scattering in (CH₃NH₃)₃Bi₂Cl₉ (MACB) Single Crystals. *Phys. Stat. Sol.* **1993**, *136*, 45. [[CrossRef](#)]
47. Kuok, M.H.; Ng, S.C.; Iwata, M.; Ishibashi, Y. A Raman study of the phase transition in (CH₃NH₃)₅Bi₂Cl₁₁. *Solid State Commun.* **1993**, *86*, 151. [[CrossRef](#)]
48. Carpentier, P. Étude des transitions de phase du cristal ferroélectrique (CH₃NH₃)₅Bi₂Cl₁₁ (PMACB): structure et dynamique Phase transitions study of the ferroelectric crystal (CH₃NH₃)₅Bi₂Cl₁₁ (MAPCB). Thesis, Université de Lille 1, Lille, France, 1995. Available online: <http://ori-nuxeo.univ-lille1.fr/nuxeo/site/esupver> (accessed on 15 May 2020).
49. Hooper, M.A.; James, D.W. Vibrational spectra of some Group Vb halides. III. A far-infrared and Raman spectral study of some Hexahalogeno-, Pentahalogeno-, and Tetrahalogeno-bismuthate(III) and -antimonate(III) salts. *Aust. J. Chem.* **1973**, *26*, 1401. [[CrossRef](#)]

